Research Article Vol. 32, No. 4 / 12 Feb 2024 / Optics Express 5783
Optics EXPRESS

Real-time millimeter wave holography with an arrayed detector

HARRY PENKETH,[1,*] M. SAID ERGOKTAS,[2] CHRISTOPHER R. LAWRENCE,[3] DAVID B. PHILLIPS,[1] JOHN E. CUNNINGHAM,[2] EUAN HENDRY,[1] AND MICHAL MRNKA[1]

[1]Department of Physics and Astronomy, University of Exeter, Exeter, Devon, EX4 4QL, UK
[2]School of Electronic and Electrical Engineering, University of Leeds, Woodhouse Lane, Leeds LS2 9JT, UK
[3]QinetiQ, Cody Technology Park, Ively Road, Farnborough, GU14 0LX, UK
[*]h.penketh2@exeter.ac.uk

Abstract: Millimeter and terahertz wave imaging has emerged as a powerful tool for applications such as security screening, biomedical imaging, and material analysis. However, intensity images alone are often insufficient for detecting variations in the dielectric constant of a sample, and extraction of material properties without additional phase information requires extensive prior knowledge of the sample. Digital holography provides a means for intensity-only detectors to reconstruct both amplitude and phase images. Here we utilize a commercially available source and detector array, both operating at room temperature, to perform digital holography in real-time for the first time in the mm-wave band (at 290 GHz). We compare the off-axis and phase-shifting approaches to digital holography and discuss their trade-offs and practical challenges in this regime. Owing to the low pixel count, we find phase-shifting holography to be the most practical and high fidelity approach for such commercial mm-wave cameras even under real-time operational requirements.

Published by Optica Publishing Group under the terms of the Creative Commons Attribution 4.0 License. Further distribution of this work must maintain attribution to the author(s) and the published article's title, journal citation, and DOI.

1. Introduction

Digital holography enables reconstruction of the phase of an electromagnetic field, using detectors that are only responsive to intensity. The principle relies on recording the intensity of the interference pattern created when an unknown field of interest interferes with a well-characterised coherent reference beam. This interference pattern encodes the phase of the unknown field, allowing it to be computationally reconstructed.

In the original realisation of holography by Gabor [1], the reference field was the unscattered object illumination, limiting the technique to the study of small, weakly scattering objects. Off-axis holography was later developed to address the limitations of Gabor holography [2,3]. Here, a separate coherent reference field is incident on the detector at an angle from the object field. However, the off-axis approach has a significant drawback in that the reconstructed image resolution is at best half of that native to the camera [4]. Later, the phase-shifting variant of holography was introduced, enabling phase information to be reconstructed at the resolution of the camera, but at the cost of requiring multiple interferogram measurements per reconstructed field [5]. Today, these three different holography techniques are commonly employed at visible frequencies, where coherent radiation sources and high resolution silicon detectors have been available for decades and the various trade-offs between holographic techniques are well understood.

While initially developed at visible frequencies, there has been particular interest in recent years in extending holography to the upper mm-wave and terahertz (THz) bands. These spectral

#513852 https://doi.org/10.1364/OE.513852
Journal © 2024 Received 21 Nov 2023; revised 10 Jan 2024; accepted 17 Jan 2024; published 2 Feb 2024

Optics EXPRESS

regions suffer from a lack of affordable electronic detectors with phase-sensitivity, in contrast to lower frequency microwave bands, where coherent detection with heterodyne receivers is more readily available [6–12]. The penetrating capabilities of millimeter and terahertz waves through many common fabrics and plastics make them attractive for non-destructive testing and security applications [13], while the non-ionizing photon energies and sensitivity to water content have motivated applications in biomedical imaging [14,15].

At low mm-wave frequencies and below, where powerful room temperature electronic sources and sensitive detectors have been developed, the diffraction limited resolution on the centimeter scale is a severe limitation for imaging. On the other hand, at high THz frequencies where resolution sub-100 μm may be achieved, even weakly absorbing materials will only permit small penetration depths [13], limiting measurements to thin samples. Here, coherent sources also either suffer from low output power requiring pulsed operation, or require bulky cryogenically cooled apparatus, such as quantum cascade lasers. Therefore there appears to be a sweet spot between high mm-wave and low THz frequencies, at around 300 GHz, where the trade-off between resolution and penetration is suited to many applications [16], and where room temperature sources with output powers in the hundreds of mW are becoming commercially available [17].

In the THz and mm-wave bands, two routes towards holography have previously been implemented. At higher frequencies (i.e. several THz), commercial pyroelectric and microbolometer detector arrays have been successfully deployed in both Gabor [18–24] and off-axis holographic imaging setups [25–31], using high power gas and quantum cascade lasers. Meanwhile, at frequencies below 1 THz, single pixel detector holography has been demonstrated using heterodyne receivers [32–37]. These methods are time-consuming, since they rely on mechanically raster-scanning a single point, amplitude-only detector across the field-of-view. We note that commercially available high resolution pyroelectric arrays may also operate as low as 0.1 THz, but their small device areas are poorly matched to the larger beam sizes and diffraction limited resolution of mm-wave imaging systems, rendering them unsuitable for holographic imaging at these lower frequencies. Meanwhile, in recent years, semiconductor-based room temperature sources and arrayed detectors have become commercially available for detection at sub 1 THz frequencies [17], permitting real-time (>1 Hz) imaging. However, the arrays tend to have a low pixel resolution, typically in the region of 16×16 pixels to 64×64 pixels, which is orders of magnitude lower than the megapixel arrays available for visible frequencies.

In this work we implement and compare the performance of two widely used holographic approaches, off-axis and phase-shifting holography, using low-pixel-count detectors. To the best of our knowledge, our work represents the first demonstration of real-time holography in the mm-wave band. We use a room temperature camera with the highest commercially available pixel count (64×64 pixels, TeraSense), tuned to operate at 290 GHz. In this low resolution regime, we explore the practical implications for both holography techniques when imaging both dielectric and metallic objects.

2. Experimental setup

Our experimental setup consists of a Mach-Zehnder interferometer with a tunable reference arm length (tuned by a translatable delay line). A partially transmitting object is placed in the signal arm of the interferometer. We study the field transmitted by the object, i.e. along the object path in Fig. 1, using an approximately 4f imaging configuration. We note that holography enables lensless reconstruction of an object from its diffracted field via digital refocusing [31,37], but that here we chose the direct imaging approach where no numerical propagation is necessary. A 290 GHz 55 mW IMPATT-diode source (TeraSense) illuminates an object plane from a distance of 200 mm. 4 inch diameter plano-convex PTFE lenses L1 and L2, with focal length f = 151 mm (Thorlabs LAT151), image the object plane onto the 290 GHz camera (TeraSense Tera-4096 64x64 pixel, 1.5 mm pitch array formed from GaAs high mobility heterostructures) [17,38]. As

Optics EXPRESS

the optics are bulky and the location of the detection plane within the camera is not precisely known, the 4f imaging configuration is adjusted to achieve a sharp image at the detection plane. The resulting separations are approximately d_1 = 135 mm, d_2 = 290 mm and d_3 = 165 mm, where d_3 is measured to the estimated location of the detector array, 10 mm behind the front face of the camera.

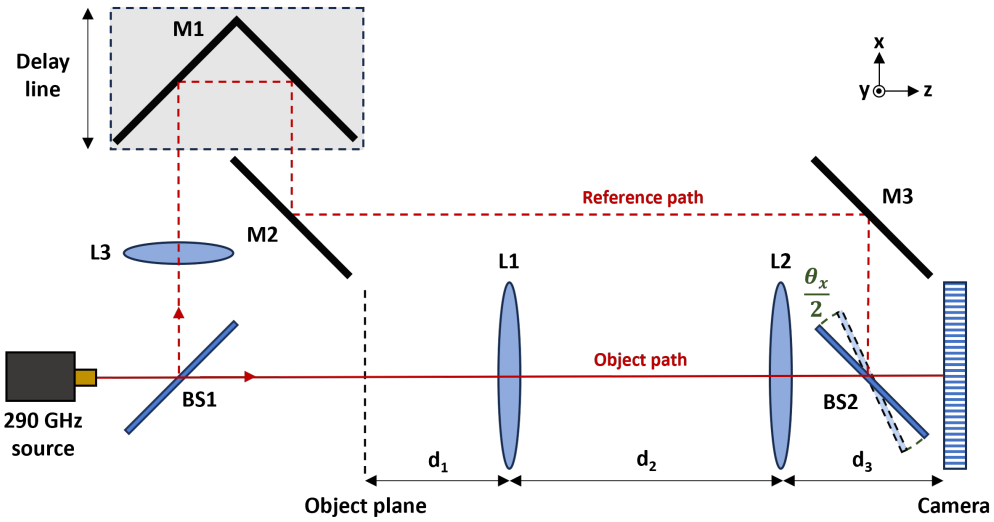

Fig. 1. Combined experimental setup for both off-axis and in-line phase-shifting digital holography. An object plane is imaged onto a mm-wave camera with a two lens system. A reference beam diverted by beam-splitter BS1, travels via a delay line (phase-shifter) onto the camera at an angle to the object beam dictated by beam-splitter BS2.

A reference beam is split from the object wave by a 675 μm thick high resistivity silicon beam-splitter (labelled BS1) just after the source. A 2 inch plano-convex PTFE lens L3 with f = 100 mm (Thorlabs LAT100), is used to reduce reference beam divergence. The reference beam then reflects off a retro-reflector M1 formed from a pair of aluminium mirrors fixed at 90° to one another mounted on a motorised translation stage, forming a delay line for the phase-shifting measurements. The delayed beam then travels via aluminium mirrors M2 and M3 to a second 675 μm thick high resistivity silicon beam-splitter BS2, which overlaps the reference and object beams onto the camera. An expanded description of the experimental setup can be found in Supplement 1 section 1.

In the off-axis approach, the reference wave must be incident at an angle ($\theta_{x,y}$) with respect to the object wave, thus creating interference fringes across the field-of-view. For phase-shifting holography, there is no requirement for an angle between the reference and object waves, and we opt for co-linear alignment between the two waves [5]. We therefore use an experimental setup in which we can easily swap between these two configurations by changing the angle of a partially reflecting mirror (BS2) before the detector. In the off-axis measurements, BS2 is rotated by half the final off-axis angle between the waves, yielding 10° about the vertical y-axis (θ_x), and 7° in the plane defined by the y and optical (z) axes (θ_y).

3. Off-axis digital holography

In off-axis digital holography, the relative tilt of a planar reference wave modulates the measured intensity of the unknown object field at a spatial carrier frequency dictated by the tilt angle. For the case of a rotation of BS2 of $\theta_x/2$ about the vertical y axis, the resulting intensity distribution

Optics EXPRESS

on the camera is [37,39]

$$I(x,y) = |E_R|^2 + |E_O(x,y)|^2 + E_R E_O^*(x,y)e^{ik\sin(\theta_x)x} + E_R^* E_O(x,y)e^{-ik\sin(\theta_x)x}, \quad (1)$$

where $E_{R,O}$ are the fields of the reference and object waves, k their free-space wavenumber and x and y are the horizontal and vertical coordinates in the camera plane respectively. An example of an interferogram produced in the off-axis configuration with $\theta_x = 10°$ and an additional tilt $\theta_y = 7°$ away from vertical, is shown in Fig. 2(a), for the two PTFE plates shown in Fig. 2(e). The impact of the spatial carrier frequency, $\nu_{x,y} = \frac{k\sin(\theta_{x,y})}{2\pi}$ is a separation of the terms of Eq. (1) in the Fourier domain, as shown in Fig. 2(b). The first two terms of Eq. (1) are real-valued, and are often known as the DC, zero order, or autocorrelation terms [4,41,42]. The signatures of these terms are centered in the Fourier plane with a radial extent twice that of the highest spatial frequencies of the object field, denoted B [41]. The field transmitted through our object E_O is diffracted into two orders located at $\pm\nu$, separated in Fourier space from the unwanted DC term and with a Fourier space radius of B.

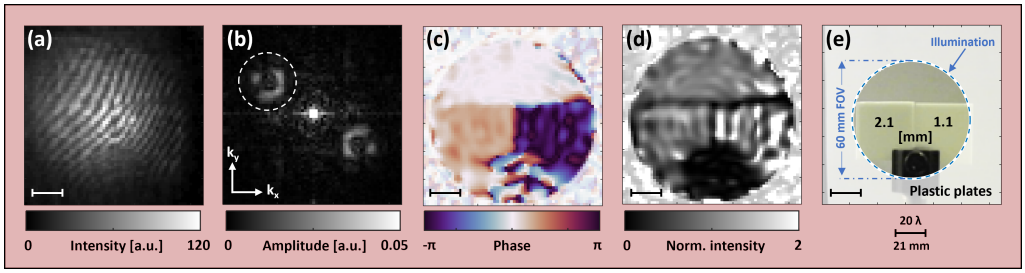

Fig. 2. Off-axis digital holography. (a) The interferogram generated between mm-wave illumination of two PTFE plates with thicknesses of 2.1 mm and 1.1 mm shown in the photograph (e) and an off-axis reference wave. (b) The amplitude of the Fourier transform of (a), with the region containing the complex object field highlighted by the dashed white circle. (c) The reconstructed phase (colormap from [40]) obtained from (b), normalised to the reconstructed phase of the illumination beam without an object. (d) As in (c), but for the reconstructed intensity. Images (c)-(e) are made 75% transparent beyond the mutually illuminated region, as a visual aid. Scale bars correspond to distances in the central, paraxial region of the object plane only, due to distortions (see Supplement 1 Fig. S2 for details).

The order located at $-\nu$, the final term of Eq. (1), can be cropped from the other terms to isolate $|E_R|E_O$ as indicated by the white circle in Fig. 2(b), here of 10 pixel radius (of 64 total in the array). The cropped region can then be shifted to the center of the Fourier plane to remove the phase gradient of the carrier wave, zero-padded and then inverse Fourier transformed. The resulting complex field $|E_R|E_O$ has the phase of E_O if E_R is well approximated by a plane wave. To remove the phase curvature of our non-planar reference wavefront, and to account for the diverging object illumination, we normalised our field reconstructions to the reconstructed field measured without the object present in the setup.

The resulting phase and intensity images for the two PTFE plates are shown in Fig. 2(c) and (d). Owing to the absence of signal at the edges of the detector array, normalised results have been made 75% transparent where the product of the reference and object wave intensities approach zero, to improve visual clarity. The refractive index of the PTFE plates can be verified from the phase images in Fig. 2(c). The resulting index, which varies spatially primarily due to the unwanted DC term contributions, ranges from ~ 1.37 to 1.48 across both plates, following $n = (\phi\lambda)/(2\pi h) + 1$, in good agreement with the literature value of ~1.43 [43,44].

We observe that the imaging system exhibits strong spherical aberrations and pincushion distortion, such that the unit magnification of the 4f imager is realised only in the central paraxial

Optics EXPRESS

portion of the field-of-view. The increasing magnification with radial distance from the optical axis is the cause of the apparent discrepancy between the field-of-view of the mm-wave images and the photographs (see Supplement 1 section 2 for details).

4. Phase-shifting digital holography

In phase-shifting digital holography [5], the phase of the object wave is inferred from the sinusoidal oscillations in pixel intensity as the phase of the reference wave is varied. We introduce this phase retardation in the reference arm, using a retro-reflector on a translation stage forming a delay line as shown in Fig. 1. This allows us to adjust the path length of the reference arm, thus globally shifting the incident phase of the reference beam compared to the object beam.

Figure 3(a) shows the interferogram formed when a mm-wave image of the metallic Siemens star shown in Fig. 3(e) is combined with a co-linear, on-axis reference beam. The two curved wavefronts produce an annular interference pattern, intersected by the minima in intensity caused by the spokes of the target. As the phase of the reference wave ϕ_R is varied via the delay line, the intensity of the pixels in the interferogram varies as [5]

$$I(x, y, \phi_R) = |E_R|^2 + |E_O(x, y)|^2 + 2\,|E_R|\,|E_O(x, y)|\cos\left(\phi_R - \phi_O(x, y)\right). \tag{2}$$

This sinusoidal variation can be seen in Fig. 3(b) for one pixel location in (a) as the delay line is moved. The object phase $\phi_O(x, y)$ is then given by the phase of the resulting sinusoid, which can be determined by fitting or temporal Fourier transform. We note that the sampling rate and range shown here far exceeds the minimum requirement for determination of the object phase (demonstrated in Supplement 1 Fig. S3), which is either three interferograms [45,46], or two interferograms and a known reference intensity [47], per reconstruction.

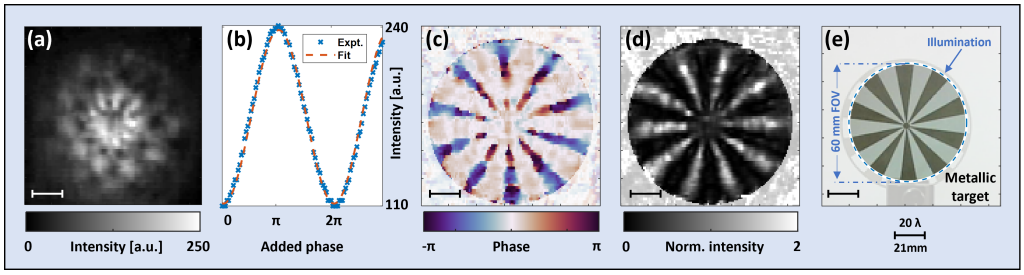

Fig. 3. Phase-shifting digital holography. (a) The interferogram generated between mm-wave illumination of a metallic Siemens star shown in the optical image (e) and an in-line reference wave. (b) The oscillation in intensity of a pixel from (a), as the phase of the reference wave is varied via a delay line. (c) The reconstructed phase obtained for each pixel as in (b), normalised to the reconstructed phase of the illumination beam without an object. (d) As in (c), but for the reconstructed intensity. Images (c)-(e) are made 75% transparent beyond the mutually illuminated region, as a visual aid. Scale bars correspond to distances in the central, paraxial region of the object plane only, due to distortions (see Supplement 1 Fig. S2 for details).

Figure 3(c) shows the reconstructed phase distribution from the sequence of interferograms recorded as the delay line travels 0.7 mm. This phase image is normalised to the equivalent phase reconstruction without an object, such that the impact of the object is shown without the phase curvature of the object and reference wavefronts. Similarly Fig. 3(d) shows the normalised intensity, i.e. the apparent transmission of the metallic target, as determined from Eq. (2) and a single measurement of the reference intensity.

Optics EXPRESS

5. Comparison of results

In Fig. 4 we compare the phase and intensity reconstructions obtained using the off-axis and phase-shifting methods. The results for each method are obtained with the optical system described in section 2 (see Fig. 1) and presented for the same two objects, a 1.0 mm thick 3D printed dielectric Siemens star (Fig. 4(a)) and a 3D printed dielectric phase plate (both Ultimaker ABS, 100% infill density). The thickness of the phase plate varies between 0 and 1.6 mm on rotation around the center point (Fig. 4(f)) and the relative permittivity of the printed material is $\varepsilon_r \sim 2.5$. This provides a controlled comparison for discussing the various trade-offs and challenges associated with the implementation of both techniques.

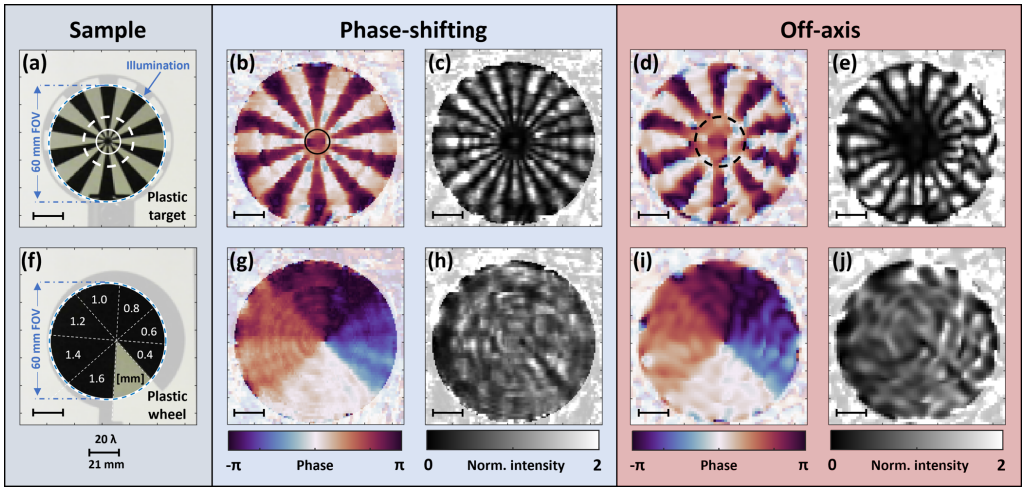

Fig. 4. Comparison between in-line phase-shifting and off-axis holography. Top row: for the 1 mm thick dielectric Siemens star shown in (a), normalised mm-wave phase and intensity reconstructions for the phase-shifting method, (b) and (c), and the off-axis method in (d) and (e) respectively. The solid and dashed circles indicate the radii at which the phase of the star's spokes meet the Rayleigh criterion, for the phase-shifting and off-axis methods respectively. Bottom row: counterparts to the top row for the dielectric phase plate shown in (f), with sector thicknesses as labelled. All images are made 75% transparent beyond the mutually illuminated region, as a visual aid. Scale bars correspond to distances in the central, paraxial region of the object plane only due to distortions (see Supplement 1 Fig. S2 for details).

5.1. Resolution

The most significant drawback of off-axis holography is the reduction in resolution that comes from Fourier filtering out of the unwanted DC and +1 diffraction orders. This process effectively reduces the pixel count of the detector array. At visible frequencies, where detector arrays commonly have millions of pixels, the off-axis reduction in image quality is typically modest, if observable. However, owing to the relatively low pixel count and large size of the available detectors at mm-wave frequencies, any effective reduction in pixel density should be considered a major drawback for imaging. In contrast, the resolution of the imaging system is maintained in phase-shifting holography.

The results of the limited imaging resolution can be seen when comparing both the intensity and phase images for the Siemens star in Fig. 4. For our imaging system, the theoretical diffraction limited object space resolution is 2.8 mm according to the Rayleigh criterion for coherent imaging. Since the magnification of our imaging system is not constant across the

Optics EXPRESS

field-of-view, as discussed in section 3 and Supplement 1 section 2, we evaluate the resolution in the central region of the images where the magnification may be approximated as unity. By locating the radius for which the spokes of the Siemens star phase images are resolved to the Rayleigh limit, marked in Fig. 4(b), we estimate the resolution of our phase image to be 2.8 ± 0.1 mm in the phase-shifting approach. However, when comparing the equivalent image from the off-axis method in Fig. 4(d), the reduction in resolution is striking. We estimate the imaging resolution in the off-axis approach to be 5.0 ± 0.2 mm using the same method.

The reduction in resolution between phase-shifting and off-axis approaches here (~ 0.5×), is less than the ratio of the 20 pixel wide Fourier filter (Fig. 2(b)) to the full (N) 64 pixel width in Fourier space, as the diffraction limited object bandwidth (B) is less than that of the camera in this configuration. This is confirmed in the calculations of the systems various spatial frequency limits in Supplement 1 section 4. The 20 pixel filter width matches well the optimised diameter of $B_{\text{opt}} = \frac{N}{(3\sqrt{2}+2)}$ [4], but the diffracted order is not ideally positioned, leading to artefacts discussed in the following section. We also note that zero-order suppression techniques may be applied to extend the maximum separable object bandwidth in the off-axis approach to half its original value [4], i.e. a 50% reduction in effective pixel density compared to the phase-shifting approach.

5.2. Artefacts

The presence of additional image artefacts in the off-axis approach is clear in Fig. 4. This is caused by the unwanted overlap between the -1 order and DC terms shown in Fig. 2(b). The off-axis angle of approximately 10° is less than needed for complete separation, which is ~ 13.5° here and would additionally require the object spatial bandwidth to not exceed B_{opt} [4]. In our system, we find the optimum tilt angle falls (somewhat awkwardly) between the small angles more suited to a tilted beam-splitter (see Fig. 1 BS2) on a standard kinematic mount and larger angles which favour direct reflection onto the camera from the final mirror (M3). Since these conditions are not perfectly satisfied experimentally, we choose a filter width which provides the best compromise between resolution and fidelity (20 pixels). This introduces additional speckle-like contributions from the DC terms into the off-axis fields, which can clearly be seen when compared with the phase-shifting images. The impact of these artefacts are partially mitigated by the much lower relative intensity of the object beam, having a spatially integrated intensity around 10% of the reference. Non-linear filtering to suppress the DC terms could reduce these artefacts further [4].

Both approaches are subject to the limitations of the imaging optics. The large spherical lenses introduce spherical aberrations and pincushion distortion, increasing the magnification at the edges of the field-of-view, which is most apparent when comparing the field-of-view in Fig. 2(c) and (e). The fine annular structure visible in both intensity and phase in the higher resolution phase-shifting results of Fig. 4(b), (c), (g) and (h), is attributed to the coherent spherical aberrations. We note that these effects are not well resolved in the off-axis case. It should also be noted that the use of imaging optics is optional in digital holography, as the diffracted fields from an object can be numerically refocused to the object plane [31,37].

5.3. Phase sensitivity

The presence of substantial artefacts in the off-axis implementation, and artefacts from the imaging optics visible with the phase-shifting approach, limit the system's ability to faithfully determine small changes in depth of a sample. In Fig. 4(b) (phase-shifting phase reconstruction), sectors of expected uniform phase shift have phase standard deviations of ~ 0.16 radians, which corresponds to a thickness value of 45 μm. In an implementation without these artefacts, the phase sensitivity will still depend on the exposure settings and associated signal to noise levels, and on the number of phase steps in the phase-shifting approach. In Supplement 1 section 5 we

Optics EXPRESS

estimate that the low bit depth of the analog to digital conversion in the camera (8-bit), would limit the minimum guaranteed resolvable depth change to ~25 μm for plastics.

5.4. Frame rate

The maximum frame rate of the (290 GHz) Tera-4096 camera is around 100 fps while the data presented here for both approaches was acquired at 14 fps, to achieve a high signal-to-noise ratio through increased integration time. Since the off-axis method relies on a single-shot measurement, the necessary data was obtained at near video frame rates and could be processed in real-time with negligible computational overhead. As proof of principle, we demonstrate holographic imaging of an oscillating pendulum at the maximum frame rate of the camera (103 fps) in supplementary Visualization 4, using the off-axis approach. Frames from the videos at a range of acquisition speeds (Visualization 1, Visualization 2, Visualization 3 and Visualization 4) and associated discussion can be found in Supplement 1 section 6. While the camera can record at rates up to 103 fps, we note that image quality degrades significantly due to noise for frame rates above 70 fps.

The key disadvantage of the phase-shifting approach to holography is speed: one requires additional measurements in order to extract phase. For our results, we over sample the phase oscillation shown in Fig. 3(b), by moving the stage at low speed and acquiring a full oscillation cycle in 5 seconds. However this exceeds the minimum requirement for determination of the object phase considerably, which can be as low as two interferograms, with a necessary phase shift dictated only by the signal-noise-ratio [47]. The fundamental speed reduction of the phase-shifting approach is then only 50% of the camera frame rate. Our tests with our motorized delay line indicate that at 14 fps acquisition rate continuous linear speeds around 2000 μm/s provide adequate sampling of the intensity oscillations. This suggests that even with a simple mechanical phase-shifter it would be feasible to record the necessary phase-shifting data set at a rate approaching only a factor of two below the read out rate of the camera, in real-time at 7 fps. We note that in the comparison presented in Fig. 4, the phase-shifting data was obtained from a large number of camera frames (101 values of phase shift), versus just one for the off-axis approach. In systems dominated by random noise this would result in a much improved signal-to-noise ratio through simple averaging, rendering the comparison unfair. However, the image quality in the off-axis approach is limited by the artefacts discussed in section 5.2 and we show in Supplement 1 Fig. S3 that the phase-shifting reconstructions are minimally degraded by reducing the sampling to just three phase values.

6. Conclusions

We have demonstrated the two leading approaches to digital holography, off-axis and phase-shifting, using a low pixel count (64×64 pixels) room-temperature detector and source operating at 290 GHz. The off-axis method yields (for our system) a resolution a factor of approximately 2 worse when compared to the phase-shifting approach under the same experimental conditions, resulting in unresolved features in the final images. In addition, the Fourier space processing inherent in the off-axis method may (as found in this demonstration) introduce additional artefacts in the reconstructed fields. In contrast, the phase-shifting approach preserves the number of the pixels in the final images and despite the necessity of multiple measurements can achieve real-time operation. This suggests that phase-shifting holography is the most practical and high fidelity approach for commercial, low pixel count mm-wave cameras even under real-time operation requirements.

For imaging highly dynamic processes prioritising frame rate over image fidelity, in applications such as high speed production line monitoring [48] the single-shot off-axis approach may be used to maximise rates and has been demonstrated in supplementary Visualization 4 at the maximal 103 fps frame rate of the camera. This is much faster than the 16 fps phase mapping

Optics EXPRESS

facilitated by recently developed THz time domain sensor arrays, though the considerably better fidelity achieved in [49,50] gives rise to improved depth sensitivity, which is hampered by holographic artifacts in our off-axis implementation. The maximum achievable frame rate for the phase-shifting approach is at best half that of the Tera-4096 camera at ~50 fps. For the higher integration times used here (with associated image signal-to-noise ratio represented in this work), the corresponding maximal 7 fps would be acceptable for most security and biomedical imaging, the two main applications of imaging in this spectral region, while the reduced impact of artefacts leads to far clearer images when compared to the off-axis approach. Moreover, the additional phase information obtained from holography would allow, for example, better contrast between dense plastics and metals in security imaging [13], or disambiguation of thickness and absorption in tissue analysis [14].

Funding. Engineering and Physical Sciences Research Council (EP/R004781/1, EP/S036466/1, EP/V047914/1); European Research Council (804626); Royal Academy of Engineering; QinetiQ.

Acknowledgements. The authors would like to thank Prof Coskun Kocabas of the National Graphene Institute at the University of Manchester for helpful conversations and access to a 100 GHz camera and source, used in preliminary experiments. The authors would also like to thank Jacopo Bertolotti for useful discussions on holography.

Disclosures. H.P.:QinetiQ Ltd (F), C.R.L.:QinetiQ Ltd (E).

Data Availability. The research data supporting this publication are openly available from the University of Exeter's institutional repository at: [51]

Supplemental document. See Supplement 1 for supporting content.

References

1. D. Gabor, "A new microscopic principle," Nature **161**(4098), 777–778 (1948).
2. E. N. Leith and J. Upatnieks, "Reconstructed wavefronts and communication theory*," J. Opt. Soc. Am. **52**(10), 1123–1130 (1962).
3. E. N. Leith and J. Upatnieks, "Wavefront reconstruction with continuous-tone objects*," J. Opt. Soc. Am. **53**(12), 1377–1381 (1963).
4. N. Pavillon, C. S. Seelamantula, J. Kühn, *et al.*, "Suppression of the zero-order term in off-axis digital holography through nonlinear filtering," Appl. Opt. **48**(34), H186–H195 (2009).
5. I. Yamaguchi and T. Zhang, "Phase-shifting digital holography," Opt. Lett. **22**(16), 1268 (1997).
6. N. H. Farhat and W. R. Guard, "Millimeter wave holographic imaging of concealed weapons," Proc. IEEE **59**(9), 1383–1384 (1971).
7. D. H. Collins, D. Mcmakin, T. Hall, *et al.*, "Real-time holographic surveillance system," (1995). U.S. Patent 5455590.
8. D. M. Sheen, D. L. Mcmakin, and T. E. Hall, "Three-dimensional millimeter-wave imaging for concealed weapon detection," IEEE Trans. Microwave Theory Tech. **49**(9), 1581–1592 (2001).
9. D. A. Robertson, P. N. Marsh, D. R. Bolton, *et al.*, *340-GHz 3D radar imaging test bed with 10-Hz frame rate*, (SPIE, 2012), pp. 836206–836211.
10. L. Qiao, Y. Wang, Z. Shen, *et al.*, "Compressive sensing for direct millimeter-wave holographic imaging," Appl. Opt. **54**(11), 3280 (2015).
11. D. Tajik, J. R. Thompson, A. S. Beaverstone, *et al.*, "Real-time quantitative reconstruction based on microwave holography," *IEEE International Symposium on Antennas and Propagation* pp. 851–852.
12. J. Gao, Y. Qin, B. Deng, *et al.*, "A novel method for 3-D millimeter-wave holographic reconstruction based on frequency interferometry techniques," IEEE Trans. Microwave Theory Tech. **66**(3), 1579–1596 (2018).
13. M. Tonouchi, "Cutting-edge terahertz technology," Nat. Photonics **1**(2), 97–105 (2007).
14. E. Pickwell and V. P. Wallace, "Biomedical applications of terahertz technology," J. Phys. D: Appl. Phys. **39**(17), R301–R310 (2006).
15. P. H. Siegel, "Terahertz technology," IEEE Trans. Microwave Theory Tech. **50**(3), 910–928 (2002).
16. R. Appleby and H. B. Wallace, "Standoff detection of weapons and contraband in the 100 GHz to 1 thz region," IEEE Trans. Antennas Propag. **55**(11), 2944–2956 (2007).
17. Terasense group inc. website, https://terasense.com/. Accessed: 2023-10-04.
18. K. Xue, Q. Li, Y.-D. Li, *et al.*, "Continuous-wave terahertz in-line digital holography," Opt. Lett. **37**(15), 3228–3230 (2012).
19. Q. Li, K. Xue, Y.-D. Li, *et al.*, "Experimental research on terahertz Gabor inline digital holography of concealed objects," Appl. Opt. **51**(29), 7052–7058 (2012).
20. H. Huang, D. Wang, L. Rong, *et al.*, "Application of autofocusing methods in continuous-wave terahertz in-line digital holography," Opt. Commun. **346**, 93–98 (2015).
21. L. Rong, T. Latychevskaia, C. Chen, *et al.*, "Terahertz in-line digital holography of human hepatocellular carcinoma tissue," Sci. Rep. **5**(1), 8445 (2015).

Optics EXPRESS

22. H. Huang, L. Rong, D. Wang, *et al.*, "Synthetic aperture in terahertz in-line digital holography for resolution enhancement," Appl. Opt. **55**(3), A43 (2016).
23. H. Huang, D. Wang, W. Li, *et al.*, "Continuous-wave terahertz multi-plane in-line digital holography," Opt. Lasers Eng. **94**, 76–81 (2017).
24. Q. Deng, W. Li, X. Wang, *et al.*, "High-resolution terahertz inline digital holography based on quantum cascade laser," Opt. Eng. **56**, 113102 (2017).
25. E. Hack and P. Zolliker, "Terahertz holography for imaging amplitude and phase objects," Opt. Express **22**(13), 16079 (2014).
26. Q. Li, S. H. Ding, Y. D. Li, *et al.*, "Experimental research on resolution improvement in CW THz digital holography," Appl. Phys. B: Lasers Opt. **107**(1), 103–110 (2012).
27. S.-H. Ding, Q. Li, Y.-D. Li, *et al.*, "Continuous-wave terahertz digital holography by use of a pyroelectric array camera," Opt. Lett. **36**(11), 1993–1995 (2011).
28. M. Locatelli, M. Ravaro, S. Bartalini, *et al.*, "Real-time terahertz digital holography with a quantum cascade laser," Sci. Rep. **5**(1), 13566 (2015).
29. M. Humphreys, J. P. Grant, I. Escorcia-Carranza, *et al.*, "Video-rate terahertz digital holographic imaging system," Opt. Express **26**(20), 25805 (2018).
30. M. Yamagiwa, T. Ogawa, T. Minamikawa, *et al.*, "Real-time amplitude and phase imaging of optically opaque objects by combining full-field off-axis terahertz digital holography with angular spectrum reconstruction," J. Infrared, Millimeter, Terahertz Waves **39**(6), 561–572 (2018).
31. Y. Zhang, J. Zhao, D. Wang, *et al.*, "Lensless fourier-transform terahertz digital holography for real-time full-field phase imaging," Photonics Res. **10**(2), 323 (2022).
32. N. H. Farhat and W. R. Guard, "Holographic imaging at 70 GHz," Proc. IEEE **58**(12), 1955–1956 (1970).
33. C. F. Cull, D. A. Wikner, J. N. Mait, *et al.*, "Millimeter-wave compressive holography," Appl. Opt. **49**(19), E67–E82 (2010).
34. M. S. Heimbeck, M. K. Kim, D. A. Gregory, *et al.*, "Terahertz digital holography using angular spectrum and dual wavelength reconstruction methods," Opt. Express **19**(10), 9192–9200 (2011).
35. W. Sun, X. Wang, and Y. Zhang, "Continuous wave terahertz phase imaging with three-step phase-shifting," Optik **124**(22), 5533–5536 (2013).
36. M. S. Heimbeck, W. R. Ng, D. R. Golish, *et al.*, "Terahertz digital holographic imaging of voids within visibly opaque dielectrics," IEEE Trans. Terahertz Sci. Technol. **5**(1), 110–116 (2015).
37. M. S. Heimbeck and H. O. Everitt, "Terahertz digital holographic imaging," Adv. Opt. Photonics **12**(1), 1 (2020).
38. V. M. Muravev and I. V. Kukushkin, "Plasmonic detector/spectrometer of subterahertz radiation based on two-dimensional electron system with embedded defect," Appl. Phys. Lett. **100**(8), 082102 (2012).
39. E. Cuche, P. Marquet, and C. Depeursinge, "Spatial filtering for zero-order and twin-image elimination in digital off-axis holography," Appl. Opt. **39**(23), 4070–4075 (2000).
40. Stephen23, "Matplotlib perceptually uniform colormaps, matlab central file exchange," https://www.mathworks.com/matlabcentral/fileexchange/62729-matplotlib-perceptually-uniform-colormaps. Accessed: 2023-10-04.
41. N. Verrier and M. Atlan, "Off-axis digital hologram reconstruction: some practical considerations," Appl. Opt. **50**(34), H136 (2011).
42. E. Sánchez-Ortiga, A. Doblas, G. Saavedra, *et al.*, "Off-axis digital holographic microscopy: practical design parameters for operating at diffraction limit," Appl. Opt. **53**(10), 2058 (2014).
43. M. N. Afsar, "Precision millimeter-wave measurements of complex refractive index, complex dielectric permittivity, and loss tangent of common polymers," IEEE Trans. Instrum. Meas. **IM-36**(2), 530–536 (1987).
44. T. Chang, X. Zhang, X. Zhang, *et al.*, "Accurate determination of dielectric permittivity of polymers from 75 GHz to 16 THz using both s-parameters and transmission spectroscopy," Appl. Opt. **56**(12), 3287 (2017).
45. G. Páez and M. Strojnik, "Phase-shifted interferometry without phase unwrapping: reconstruction of a decentered wave front," J. Opt. Soc. Am. A **16**(3), 475–480 (1999).
46. L. Z. Cai, Q. Liu, and X. L. Yang, "Phase-shift extraction and wave-front reconstruction in phase-shifting interferometry with arbitrary phase steps," Opt. Lett. **28**(19), 1808 (2003).
47. X. F. Meng, L. Z. Cai, X. F. Xu, *et al.*, "Two-step phase-shifting interferometry and its application in image encryption," Opt. Lett. **31**(10), 1414–1416 (2006).
48. L. A. Downes, A. R. MacKellar, C. S. Adams, *et al.*, "High-speed THz imaging for production line monitoring," (IEEE, 2019), pp. 1–2.
49. X. Li, D. Mengu, A. Ozcan, *et al.*, "16 frames-per-second terahertz time-domain imaging through a plasmonic photoconductive focal-plane array," (Institute of Electrical and Electronics Engineers Inc., 2023), pp. 566–569.
50. X. Li, D. Mengu, N. T. Yardimci, *et al.*, "Plasmonic photoconductive terahertz focal-plane array with pixel super-resolution," Nat. Photonics (2024).
51. H. Penketh, E. Hendry, D. Phillips, *et al.*, "Data for: Real-time millimeter wave holography with an arrayed detector," University of Exeter: Version 1, 2024, https://doi.org/10.24378/exe.4986.